Title

Lithium-Metal Batteries: Enabling Rapid Charging Lithium Metal Batteries via Surface Acoustic Wave-Driven Electrolyte Flow (Adv. Mater. 14/2020)

Journal

Advanced Materials, 32(14)

ISSN

0935-9648

Authors

Huang, An
Liu, Haodong
Manor, Ofer
et al.

Publication Date

2020-04-01

DOI

10.1002/adma.202070108

Peer reviewed

Enabling rapid charging lithium metal batteries via surface acoustic wave-driven electrolyte flow

An Huang,[†] Haodong Liu,[‡] Ofer Manor,[¶] Ping Liu,[‡] and James Friend[*,†]

†*Materials Science and Engineering Program and the Department of Mechanical and Aerospace Engineering, University of California San Diego, 9500 Gilman Drive, La Jolla, CA 92093 USA*

‡*Materials Science and Engineering Program and the Department of Nanoengineering, University of California San Diego, 9500 Gilman Drive, La Jolla, CA 92093 USA*

¶*Wolfson Department of Chemical Engineering, Technion—Israel Institute of Technology, Haifa, Israel*

E-mail: jfriend@eng.ucsd.edu

Abstract

Both powerful and unstable, practical lithium metal batteries have remained a difficult challenge for over fifty years. With severe ion depletion gradients in the electrolyte during charging, they rapidly develop porosity, dendrites, and dead Li that cause poor performance and, all too often, spectacular failure. Remarkably, incorporating a small, 100-MHz surface acoustic wave device (SAW) solves this problem. Providing acoustic streaming electrolyte flow during charging, the device enables dense Li plating and avoids porosity and dendrites. SAW-integrated Li cells can operate up to 6 mA/cm^2 in a commercial carbonate based electrolyte; omitting SAW leads to short circuiting at 2 mA/cm^2. The Li deposition is morphologically dendrite-free and

close to theoretical density when cycling with SAW. With a 245 μm thick Li anode in a full Li‖LFP ($LiFePO_4$) cell, introducing SAW increases the uncycled Li from 145 μm to 225 μm, decreasing Li consumption from 41% to only 8%. A closed-form model is provided to explain the phenomena and serve as a design tool for integrating this chemistry-agnostic approach into batteries whatever the chemistry within.

The rechargeable battery is the key to improving a broad swath of technology for society, from consumer and defense electronics, grid energy storage, and robotics to electric vehicles for sustainable transport.[1,2] Properties in safety, rechargeability, specific capacity, and lifetime still need improvement: the best lithium ion battery today (240 Wh/kg) offers only six times the energy density of a lead-acid battery (40 Wh/kg) from 120 years ago.[3–5] As current state of the art Li-ion batteries (LIB) approach their theoretical limits by using lithiated graphite and meticulously engineered electrolytes, alternatives are sought to increase the energy density in batteries for emerging electronic devices.[6] Lithium metal (Li) is the ideal choice as an anode in Li metal batteries (LMB) with a potential to deliver an energy density of 500 Wh/kg, at least double the current LIB.[1] The decision in the 1980s to abandon LMBs after years of research and adopt LIBs was in recognition of the difficult problem of dendrites forming on the Li metal anode during recharging. The dendrites will not only penetrate the separator and lead to serious safety issues but also will lead to low Coloumbic efficiency and a substantial reduction in charge capacity as they consume both Li and electrolyte.[7] These issues have long impeded commercialization of Li metal batteries (LMB) despite their otherwise overwhelming advantages.[8,9]

Beyond chemistry, external magnetic forces have also been proposed to inhibit continuous growth of the dendrite tips through magnetohydrodynamics.[10,11] However, the energy consumption is high and the performance is limited. Ultrasound has been used to drive acoustic streaming-driven fluid stirring and enhance the uniformity of ion distribution during traditional chemical vapor deposition.[12,13] However, the ultrasonicators in these past works have always been large, inefficient, electrochemically incompatible, and very heavy—unsuitable for integration into a practical LMB. By contrast, surface acoustic wave (SAW) devices offer extraordinary power density in a fingernail-sized device, and are useful in drop handling, biological sensors, cell manipulation, and particle collection in microfluidics.[14–17] Uniquely, they generate locally extreme accelerations of 10^8 to 10^{10} m/s^2, driving acoustic streaming-driven fluid flow at up to 1 m/s, and imparting acoustic forces upon objects present in the fluid, such as cells and micro to nano-scale particles.[18] SAW devices can be inexpensively produced through

a standard ultraviolet photolithography and lift-off process to deposit interdigitated metallic electrodes onto a low-loss, single crystal piezoelectric Li niobate substrate, a commodity from decades of development and use in telecommunications.[19]

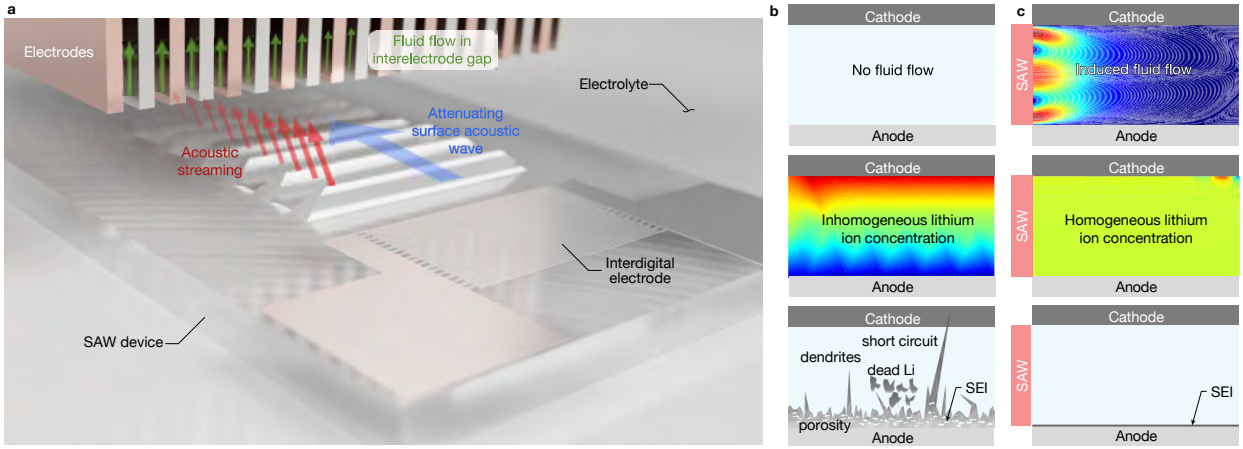

Figure 1: **A comparison of the working principles of traditional and SAW-driven Li metal batteries. a,** Illustration of how acoustic streaming drives electrolyte flow in the gap(s) between the electrode(s). A **b,** traditional LMB compared to **c,** SAW LMB based upon computations of the flow and ion distribution. For a traditional LMB, the stationary electrolyte permits high ion concentration gradients to appear during charging, producing Li dendrite formation, dead Li, Li metal volume expansion, uneven solid electrolyte interface (SEI) formation, and, eventually, short circuit of the cell. By contrast, in a SAW LMB, acoustic streaming recirculates the electrolyte, leading to a homogeneous ion distribution and uniform Li deposition during charging.

In this work, we expect to overcome the two underlying problems hampering rechargeable battery progress for over fifty years: protracted charging times and inadequate lifetime due to unfavorable morphological changes. We especially seek to avoid Li dendrites when metal deposition processes are employed in a carbonate-based electrolyte, EC/DEC, which is notorious[20] for Li dendrite formation and caused by ion depletion in the electrolyte adjacent the anode. A SAW-integrated LMB (SAW LMB) is therefore proposed, as shown in Fig. 1, as a new route to potentially overcome these longstanding problems. By driving sufficient flow of the electrolyte through the interelectrode gap, it becomes possible to prevent the formation of Li ion depletion regions, thus preventing dendrites, adverse heating, and electrolyte breakdown. The flow is driven by acoustic (fluid) streaming generated by the SAW device, significantly reducing the Li concentration gradient in the electrolyte—even during rapid charging—and uniform Li de-

position is made possible. The power consumption of the SAW device is around 10 mWh/cm^2, relatively small in comparison to the charging itself, and in any case occurring when power consumption is acceptable: during charging. During LMB discharge, dendrites do not form, and so the SAW device may remain off. In what follows, we report the results of galvanostatic cycling and post cycling analysis of prototype Li metal batteries to describe the beneficial effects of using SAW in them. Furthermore, we provide a closed-form model that both describes the underpinning physics and can be used to design the SAW device for a given battery configuration.

Li deposition onto copper in the presence of SAW

We first consider the Li deposition morphology on a copper (Cu) substrate using a carbonate based electrolyte of 1M $LiPF_6$ in ethylene carbonate/dietheryl carbonate (EC/DEC; Fig. S3). The carbonate electrolyte was chosen as our baseline electrolyte because it is known to be compatible with 4 V cathode materials and is capable of triggering dendrite formation at current densities of only 0.5 mA/cm^2 in an Li anode cell.[21,22] The Li was electrochemically plated onto the Cu substrate at a current density of 1 mA/cm^2 (1 C) until the areal capacity reached 1 mAh/cm^2 for both baseline and SAW Li‖Cu cells (the deposition profile is shown in Fig. S3a). The voltage of the baseline cell continued to decrease as Li was deposited, while the SAW cell exhibited a constant voltage near -0.1 V, indicating stable electrodeposition and perhaps homogeneous deposition.[23] Upon increasing the deposition current density to 6 mA/cm^2 (6 C) for cells with and without SAW (Fig. S3b), similar trends were observed. A more drastic drop in the deposition voltage was observed in the early stage of the deposition for the baseline cell, followed by a continued drop from -0.3 V at 0.1 mAh to -0.58 V at 1 mAh. In contrast, the SAW Li‖Cu cell showed a nearly identical voltage profile, becoming constant at -0.1 V. Notably, the baseline cell exhibited a deep voltage drop at the beginning of the 6 mA/cm^2 deposition (circled in Fig. S3b). This phenomenon has been seen before and is associated with the overpotential due to a het-

erogeneous nucleation barrier from the thermodynamic mismatch between Li and Cu,[24] and appears to be absent when using SAW.

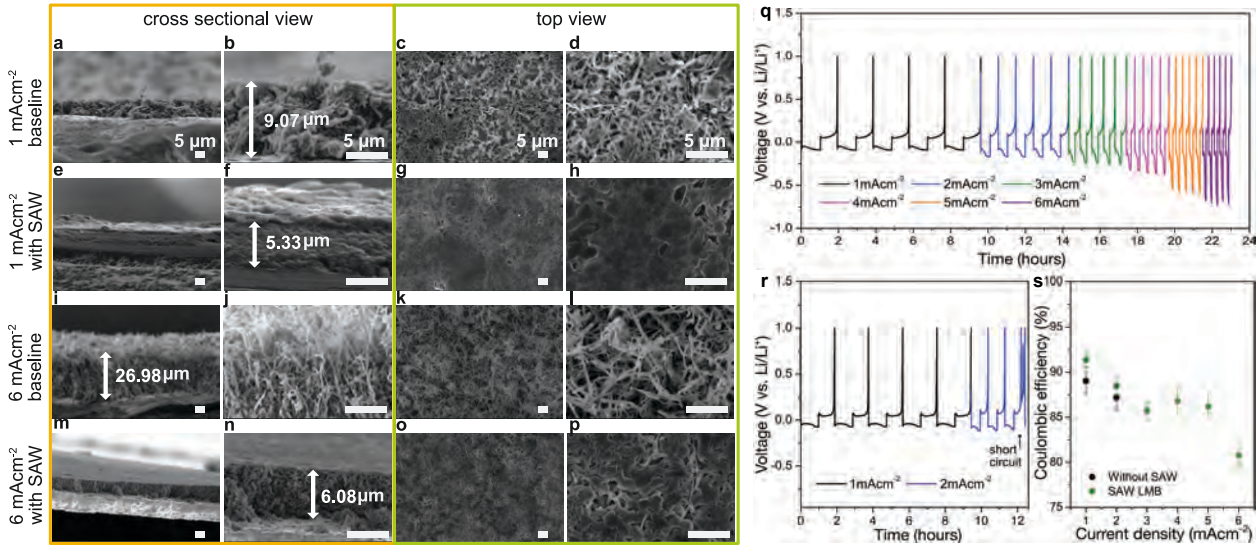

Figure 2: **SEM images of the Cu electrodes in the Li‖Cu system with and without SAW after the first deposition cycle.** Images of the Cu electrode after plating 1 mAh/cm^2 areal capacity of Li under 1 mA/cm^2. **a-d** the baseline Li‖Cu system shows substantially different morphology than **e-h** with SAW under the same conditions. Images of the Cu electrode after plating 1 mAh/cm^2 areal capacity under 6 mA/cm^2. **i-l** baseline and **m-p** SAW-driven Li‖Cu cell. Note the views among each column are at the same scale, with **a,b,e,f,i,j,m,n** cross-sections and **c,d,g,h,k,l,o,p** top views of the Cu electrode. Moreover, the comparison of Coulombic efficiency of Li‖Cu batteries with and without SAW at various deposition and stripping rates. The testing current densities incrementally progressed from 1 mA/cm^2 to 2, 3, 4, 5, and 6 mA/cm^2 until—in each case—the deposition reached areal capacity of 1 mAh/cm^2 and was stripped back to 1 V, producing an electrochemical profile of the Li‖Cu cell **q,** with SAW and **r,** without SAW. The **s,** average Coloumbic efficiency of the baseline (black dots) and SAW-driven Li‖Cu (green dots) are shown as a function of the current density.

The cycled cells were then disassembled and the electrodes were collected for scanning electron microscopy (SEM). When cycled at 1 mA/cm^2 current density, the presence of SAW reduces the thickness of the deposited Li from 9.1 μm without SAW in the baseline cell to 5.3 μm with SAW. The thickness of the deposition is an indication of its density. A 4.85 μm thickness may theoretically be achieved if the deposition is completely dense without porosity or dendrites.[25] While the SEI is a factor, its volume is insignificant compared to the dead Li present in the battery based on recent published data.[26] Based on these values, the porosities of the deposited

Li are 46.7% and 8.5% for the baseline cell and SAW cell, respectively. The Li‖Cu cell produces better deposition behavior with SAW than without it. The top view images further support this conclusion, as the deposition morphology is dense and without dendrites for the SAW Li‖Cu cell (Fig. 2g and 2h) while porosity and dendrites are present in the baseline Li‖Cu cell (Fig. 2c and 2d).

We further examined the Li‖Cu cells' electrodes after Li deposition at a current density of 6 mA/cm^2. The Li deposition thickness in the baseline cell increased three-fold from 9.1 μm to 27 μm, giving an extremely high porosity of 82%, an indication of dendrite formation and loose deposition.[27] By comparison, the deposition thickness is far less when using SAW, 6 μm, with a much lower porosity of 19%. Though the porosity is certainly higher at 6 mA/cm^2 than 1 mA/cm^2, using SAW produces far better deposition behavior. Again, the top view images support this conclusion, with substantial porosity and dendrites in the cell without SAW (Fig. 2k, and 2l) and homogeneous "chunked" morphology with SAW (Fig. 2 and 2,p) known to result from homogeneous current distribution during deposition.[28]

Moreover, we investigated the deposition morphology of Li on Cu after charging to 1 mAh/cm^2 charge capacity at a current density of 6 mA/cm^2 while using SAW input powers of 40 mW and 500 mW, less and greater, respectively, than the 100 mW used in Fig. 2. At low SAW input power (40 mW), the thickness of Li at 6 mAh/cm^2 is 8.75 μm (Fig. S4a,b). The deposition thickness is greater than the 6.08 μm deposition thickness obtained at a SAW power of 100 mW (Fig. 2n). However, it is much thinner than the 27 μm of Li deposited in the baseline cell (Fig. 2i). Moreover, viewed from the top, the Li morphology is a mixture of dendrites and chunks (Fig. S4c,d), indicating that when an insufficient power is applied, the effect of acoustic streaming on the Li^+ concentration gradient is limited, resulting in a less dense Li deposition. However, increasing the SAW input power to 500 mW produces a 7.5 μm thick layer of Li (Fig. S4e,f), between the deposition thicknesses found when using 40 mW (8.75 μm) and 100 mW (6.08 μm). The deposition morphology at 500 mW SAW power is a chunk-like structure (Fig. S4g,h).

We also examined the Coulombic efficiency of the Li‖Cu cell with the same carbonate elec-

trolyte at different current densities, both with and without SAW (Fig. 2q and 2r). At 1 mA/cm^2 and 2 mA/cm^2, the average Coulombic efficiencies are 91.5% and 89% with SAW, nearly identical to the baseline cell without SAW, at 88% and 87%, respectively. However, at 2 mA/cm^2 the baseline cell exhibits signs of a short circuit with an unstable electrochemistry profile in the third cycle. By contrast, the SAW Li‖Cu cell continues to show good cycling performance even to the extremely high cycling rate of 6 mA/cm^2, maintaining >80% Coloumbic efficiency throughout.

Effect of SAW-driven fluid flow on the high rate performance of Li‖$LiFePO_4$ batteries

We assembled a full Li‖$LiFePO_4$ (Li‖LFP) cell to investigate the practical aspects of integrating a SAW device into a battery, using LFP as the cathode with an areal capacity of 1 mAh/cm^2. The effect of SAW on the high charge rate capability of Li‖LFP cells is illustrated in Fig. 3 using 1M $LiPF_6$ in EC/DEC carbonate electrolyte at different current densities. Both charge and discharge are conducted at the same current density for this test. At a low current density of 0.5 mA/cm^2(0.5 C), both the baseline Li‖LFP cell and SAW Li‖LFP cell exhibit a discharge capacity of about 137 mAh/g, due to the small Li^+ concentration gradient present in the electrolyte at this current density, whether or not SAW is circulating the electrolyte. As the current density increases beyond 1 mA/cm^2 (1 C), however, a visible difference appears in the charge/discharge capacity due to the SAW. At 1 mA/cm^2, the capacity is 120 mAh/g without SAW, and 130 mAh/g with SAW. Notably, 1 mA/cm^2 is reported as the critical current density that, upon exceeding, dendrites start to grow and the limitations of Li^+ ion diffusion begins to impact the battery's cycling performance.[4]

As the current density is further increased to 6 mA/cm^2(6 C), the discrepancy in capacity likewise grows due to the SAW. The baseline cell delivered only 11 mAh/g, retaining only 8% of its low-rate capacity, but using SAW in the cell provides a discharge capacity of 55 mAh/g, re-

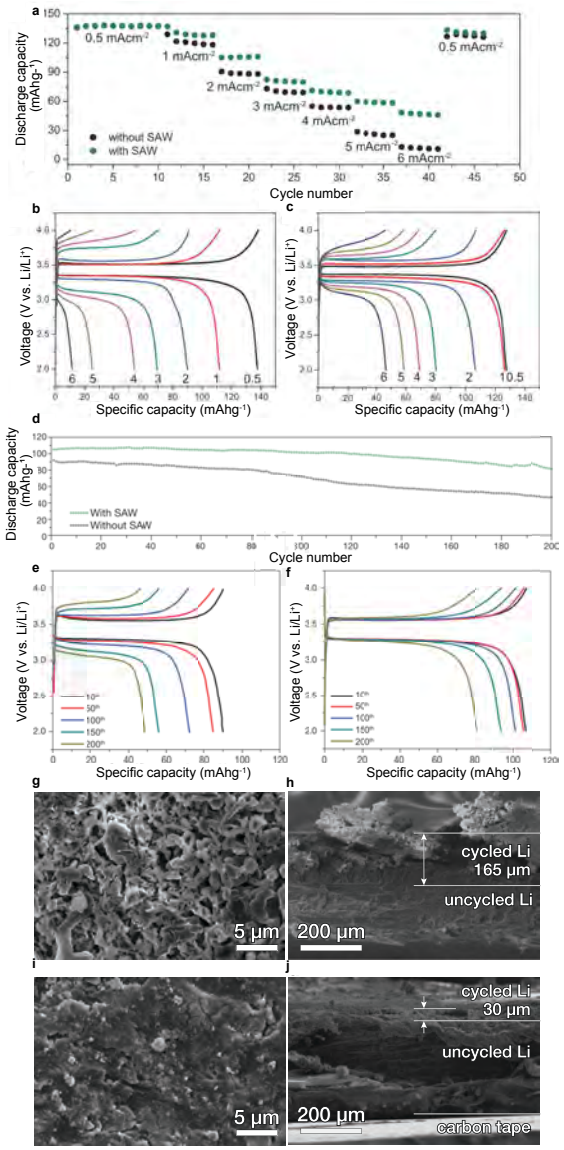

Figure 3: Electrochemical properties of baseline and SAW-driven Li‖$LiFePO_4$ cells at different cycle rates and long term cycleability. **a,** The discharge capacities of the baseline (black) and SAW-driven (green) Li‖$LiFePO_4$ cells are plotted versus the charge/discharge cycle at progressively greater current densities of 0.5, 1, 2, 3, 4, 5, and 6 mA/cm^2 (1 mA/cm^2 corresponds to 1 C)). The representative charge and discharge voltage profiles of Li‖$LiFePO_4$ cells are likewise shown for current densities of 0.5, 1, 2, 3, 4, 5, and 6 mA/cm^2 in the **b,** baseline and **c,** SAW Li‖$LiFePO_4$ cells. **d,** The discharge capacity of an Li‖LFP with (green) or without (black) SAW over 200 cycles at a current density of 2 mA/cm^2. The associated charge and discharge profiles of the **e,** baseline and **f,** SAW Li‖LFP cells are plotted at cycles 10, 50, 100, 150, and 200. Scanning electron microscopy of the morphology of Li in the Li‖LFP cell after 200 cycles. Extensive porosity and dendrites are present in a **g,** top view and **h,** cross sectional view of the Li anode from the SAW-absent Li‖LFP baseline cell, unlike the comparatively dense and smooth morphology of the Li anode from the SAW Li‖LFP cell (**i,** top view and **j,** cross sectional view).

taining 40% of its low-rate capacity. The SAW provides a five-fold increase in discharge capacity at 6 mA/cm^2 (6 C). Finally, each cell was returned to the starting current density of 0.5 mA/cm^2 (0.5 C), and the capacity was found to recover—indicating an absence of battery damage from the fast charge and discharge cycling. The SAW Li‖LFP generated a slightly higher capacity than the baseline Li‖LFP. Altogether, the drop in capacity at 6 mA/cm^2 (6 C) is mainly due to the limited Li^+ ion diffusion rate, producing a corresponding large Li ion concentration gradient. Without SAW, it is not possible to charge the Li‖LFP at high current densities. But with SAW, the discharge capacity is improved despite the high current density, perhaps due to improvement of the Li^+ ion diffusion and reduction of the associated ion concentration gradient via SAW-driven electrolyte recirculation.

The limitations in Li^+ diffusion can be shown in the charge and discharge profiles of the baseline Li‖LFP (Fig. 3b) and SAW Li‖LFP (Fig. 3c). At high cycle rates, the voltage hysteresis dramatically increased in the baseline Li‖LFP cell to 1.02 V at 6 mA/cm^2 (6 C) current density, 70% larger than the SAW Li‖LFP (0.59 V). The large voltage hysteresis is again an indication of the poor Li ion transportation in the baseline cell. Since the initial voltage hysteresis is similar for the cell with or without SAW, the resistance otherwise present in the cell is likewise similar.

Full cell cycling of Li‖LFP with and without SAW

The long term cycling stability of the SAW Li‖LFP cells was investigated by applying a current density of 2 mA/cm^2 (2 C) for both charge and discharge over 200 cycles to Li‖LFP cells, using cut-off voltages of 2–4 V. The discharge capacity plotted in Fig. 3d–f indicates superior cycle performance with SAW in the Li‖LFP cell, with a greater discharge capacity throughout, from the initial to the 200th cycle. With SAW, the Li‖LFP offers 110 mAh/g of discharge capacity, modestly more than the 90 mAh/g of the baseline Li‖LFP without SAW. After 200 cycles, however, the SAW Li‖LFP cell retained 82% of its initial discharge capacity after 200 cycles, far more than the 51% capacity retained by the baseline Li‖LFP cell.

The effect of SAW is further apparent in a comparison between the individual charge and discharge voltage profiles of the baseline Li‖LFP in Fig. 3e and the SAW Li‖LFP cell in Fig. 3f. The baseline cell's polarization increases with the number of cycles, and there is a 63% increase in the polarization voltage from the 10^{th} cycle (0.28 V) to the 200^{th} cycle (0.77 V). The increase in polarization is an indication of dead Li and Li dendrite formation,[27] leading to a reduction in discharge capacity as cycles accumulate. However, with SAW, the polarization voltage increases less than 10% from 0.266 V at the 10^{th} cycle to 0.298 V at the 200^{th} cycle, indicating the achievement of stable cycle performance using SAW.

The cycled Li‖LFP cells were disassembled to examine the morphology of the Li anodes using scanning electron microscopy (SEM, Fig. 3g–j and Suppl. Fig. S5). The Li anode from the baseline cell exhibits porous morphology and dendritic growth in Fig. 3g,h. However, with SAW, the Li anode morphology is comparatively dense and smooth in Fig. 3i,j. Noting the total thickness of the pristine Li is 245 μm, this substantial difference may be quantified by measuring the thickness of the (porous) cycled Li and (dense) uncycled Li using Fig. 3i,j. The thickness of the uncycled Li is 145 μm without SAW, and is 225 μm with SAW. In the baseline Li‖LFP cell without SAW, 41% of the Li participates in the cycling. The thickness of the cycled Li increased from 100 μmm to 165 μm after 200 cycles without SAW, a 65% increase. By contrast, with SAW in the Li‖LFP cell, only 8% of the Li is cycled, and the cycled Li increased from 20 μm to 30 μm after 200 cycles, a 33% increase.

The mechanism responsible for SAW-driven battery performance improvement

The diffusion of Li^+ ions is crucial to the performance of Li batteries: its charge and discharge rate, capacity, and stability. Most batteries have quiescent electrolyte, with $u = 0$ for the electrolyte velocity, leaving diffusion to migrate Li^+ ions across concentration gradients in the electrolyte and to the anode during charging (Fig. 1b).[29] Diffusion is inadequate in high-speed

charging, and by generating flow in the electrolyte, SAW-driven acoustic streaming *augments* diffusion—in fact supplants it—in transport of Li^+ ions (Fig.1c), but the details require careful analysis summarized here and provided in more detail in the Supplementary Information.

Past analyses typically employ spatially one-dimensional models,[29,30] as the full problem is not easy to solve, even with a computer.[31] Here, we seek an immediately useful, closed-form result to both explain the physical phenomena and provide a tool for battery design incorporating SAW-driven electrolyte recirculation, examining how flow inhibits the early growth of small dendrites, as suggested by classic experimental work on impinging flow.[32]

We assume the cell is near its limiting current density, the worst case scenario for dendrite formation. We further assume that slight, sinusoidal morphological imperfections are present along the electrode—of wavelength λ and amplitude ϵ from the initial construction of the battery (*see* Sup. Fig S6)—forming "hotspots" that locally enhance the rate by which metal ions adsorb onto the electrode and allow for the initial growth of dendrites. With our electrolyte, the Reynolds number is $\mathrm{Re} = \rho u L/\mu \approx 0.2-2$, as a function of the density ρ, viscosity μ, and length scale L, indicating laminar, almost viscous, flow as one might expect from the dimensions of the structure, though the Li^+ ion convection is strong, potentially with an ion transport boundary layer of $\ell \approx 0.1-1$ μm thickness, as the diffusion coefficient[33] is ~10^{-9} m^2/s, due to the requirement that the leading order convective and diffusive components in the transport equations must become comparable in magnitude within the boundary layer, in turn satisfied by requiring that the corresponding Peclet number in the boundary layer is $\mathrm{Pe} = u_c \ell / D \approx 1$ in a simplified analysis assuming the electrolyte flows as a simple shear flow with characteristic velocity u_c. The small thickness of the boundary layer compared to the interelectrode gap, and the lack of excess pressure therein supports—at least locally—our simple shear flow assumption. It is similar to a past successful approximation[34] of a parabolic velocity profile between flat and parallel electrodes as simple shear flow in the boundary layer near the electrodes.

By modeling the advective and diffusive transport of ions, both transverse and parallel to an electrode in the cell, as a two-dimensional convection-diffusion model as detailed in the

Supplementary Information, we connect the acoustically-driven electrolyte flow in the cell to the ion distribution in the vicinity of these hotspots. The connection is made via an order-of-magnitude result that defines the Li ion adsorption onto the anode during charging:

$$\frac{-i}{\mathrm{Pe}^{1/3} D c_{\mathrm{bulk}}/\delta} = \frac{3^{1/3}(1-\epsilon)}{\Gamma(1/3)}\left(\frac{x}{\delta}\right)^{-1/3} + \epsilon\frac{\sqrt{\pi}(3/2)^{1/3}}{\Gamma(1/6)}(k\delta)^{1/3}\left(\sin(kx)-\sqrt{3}\cos(kx)\right) + \mathcal{O}[\epsilon], \quad (1)$$

The SAW-driven mechanism reducing dendrite growth and facilitating dense Li plating is counterintuitive. Acoustic streaming driven by SAW causes fluid flow in the interelectrode gap. During charging, the Li^+ ion flux is generally enhanced by the flow as indicated by the first of the two terms on the right-hand side of eqn. (1). However, this spatially ($x^{-1/3}$) decaying ion flux is perturbed by the second term on the right-hand side of eqn. (1), which represents the variation in ion flux due to the presence of localized hotspots that arise from the initial electrode roughness. The combined contribution of both terms indicates the key to eliminating the possibility of dendrite growth: the dominance of the first term over the second. We seek the critical length, x_{crit}, over which the spatially oscillatory behavior of the second term is suppressed by requiring the change in ion absorption current, i, with respect to x, $d(-i)/dx > 0$. This avoids a sign change in the current and localized regions of enhanced ion flux—hotspots that will lead to dendrites and porous deposition. With some effort, the critical length $x_{\mathrm{crit}} \approx \lambda\sqrt{\mathrm{Pe}}/18$.

The effect of the flow via the Peclet number Pe is to produce a region of size x_{crit} over which nonuniform ion deposition is prevented. The size of this region depends upon the wavelength of the initial roughness, $\lambda = 200\mu$m, both an artificial construct to avoid lengthy computations in favor of useful, analysis-based design tools and a fair representation of as-supplied, pristine Li surface morphology as indicated in Sup. Fig S6. The Peclet number linearly depends upon the acoustic streaming flow, and this helps us define the characteristics required from the SAW device to ensure the critical length is at least equivalent to the battery size—$L_{\mathrm{bat}} \sim 10$ mm in our case.

If we equate $x_{\mathrm{crit}} \approx L_{\mathrm{bat}}$, and substitute in the definition for the Peclet number, we may

identify the necessary flow velocity required to avoid nonuniform ion deposition over a region equivalent to the size of the battery, $u_{c,\mathrm{crit}} \approx D(18L_{\mathrm{bat}}\lambda)/\ell \sim 0.1$ m/s in our system. This allows us to determine the SAW input power required[35] to suppress dendrites throughout, $P_{\mathrm{crit}} = \rho\alpha w c u_{c,\mathrm{crit}}^2 \sim 0.1$ W, where $\alpha = 455$ μm refers to the attenuation length of the SAW in the fluid-loaded LN substrate, $w \sim 10$ mm is the aperture or width of the SAW, $c = 1498$ m/s is the speed of sound in the electrolyte, and $\rho = 998$ kg/m^3 is the electrolyte density. We may also determine the ideal frequency to use for the SAW by equating the attenuation length of the acoustic wave, β, to the battery size, $\beta = L_{\mathrm{bat}}$. This ensures locally generated acoustic streaming throughout the battery, helping to overcome the presence of the separator and still induce fluid flow over the entire interelectrode gap. The frequency is $f_\beta = \sqrt{\left(\rho c_{\mathrm{SAW}}^3\right) / \left[4\pi^3\left(\mu+\mu'\right)L_{\mathrm{bat}}\right]} \sim 10^8$ Hz, the reason we choose 100 MHz in this study. The speed of the Rayleigh wave SAW in the LN substrate is $c_{\mathrm{SAW}} = 3900$ m/s and the dynamic and dilatational viscosities of the electrolyte are, respectively, $\mu = 1$ s-mPa and $\mu' = 3$ s-mPa. These values are consistent with our experimental observations in the ability to suppress nonuniform Li^+ ion deposition with SAW in prototype Li metal batteries.

Conclusions

We have devised a chemistry-agnostic means for avoiding ion depletion and dendrite growth in liquid electrolyte batteries. Adopting small, high-frequency ultrasound generators to drive electrolyte flow within the inter-electrode gaps gives rise to ion flux distributions that render potential locations of dendrite growth stable within a specific distance from the ultrasound source. This distance is independent of the details of the flow as long as the Peclet number is sufficiently large. This is fortunately possible with the acoustic streaming induced by our ultrasound devices and make practical Li metal rechargeable batteries possible, even with rapid charge rates and the choice of electrode materials and electrolytes that would normally be considered unrealistic. The Li‖Cu configuration, as an example, was able to cycle until 6 mA/cm^2

current density with reasonable Coulombic efficiencies above 80% throughout. Moreover, the Li‖$LiFePO_4$ configuration can deliver 95 mAh/g capacity after 200 cycles at 2C charge and discharge rates. Dense plating of Li in both cell types was shown with SAW, and compared to the significant porosity and dendrites present in otherwise identical cells without SAW.

We anticipate a remarkable freedom in the choice of battery electrochemistry and operation to be facilitated from this simple technology, enabling greater efficiency, utility, and sustainability of rechargeable batteries for a broad swath of current and future applications.

Methods

Cell and SAW device fabrication

Copper (10 μm thick, MTI Corporation) was immersed in 1 M HCl followed by rinsing first with water and then with acetone to remove surface impurities and oxides before use as electrodes in all experiments. The Li (250 μm thick, MTI Corporation) was carefully scraped (245 μm thick after scraping) to remove any oxide layers before use as electrodes in all experiments. The lithium iron phosphate (LFP) electrode was prepared by first mixing LFP powder (MTI Corporation), polyvinylidene fluoride (Sigma Aldrich), and carbon black (C-preme LLC) in the mass ratio of LFP:PVDF:C= 75% : 10% : 15%; then made into a slurry by mixing with N-methyl-2-pyrrolidone (Sigma-Aldrich) as a solvent; pour-cast on Al foil; and finally dried in a vacuum oven for 12 hours. The areal capacity is around 1 mAh/cm^2. Commercial grade 1M solution of lithium hexafluorophosphate ($LiPF_6$) in a 1:1 (w/w) mixture of ethylene carbonate (EC) and diethyl carbonate (DEC) (BASF) was used as the electrolyte. Finally, a Celgard 480 separator was used between the cathode and anode.

The SAW device was fabricated through lift-off lithography to deposit twenty-eight pairs of unweighted Au/Cr fingers and form an optimal[14] interdigital transducer (IDT) onto a 500 μm thick 127.68° Y-rotated, X-propagating cut lithium niobate substrate ($LiNbO_3$ (LN), Roditi).[17,18] The SAW device was then coated with parylene C using chemical vapor deposition (PDS 2010

parylene coater system, Specialty Coating Systems) to prevent reactions with the electrolyte (see Suppl. Information). The baseline LMB and SAW-integrated LMB were assembled inside an argon-filled glovebox (MTI Corporation), where the moisture level and O_2 level were both <1 ppm. Both the baseline and SAW LMB cells were formed from perfluoroalkoxy alkane nuts, back and front ferrules, and main housings (PFA-820-6, Swagelock) in conjunction with current collectors (304 stainless steel rods, McMaster-Carr Supply Corporation), as illustrated in Fig. S2, to both seal the electrolyte and electrode from exposure to air and to safely test the cells.

Electrochemical measurement

Electrochemical studies were carried out in the Swagelock-based cell, placing the SAW device on one side within the housing and perpendicular to the electrode gap as shown in Fig. S2. The Coulombic efficiency measurements during Li plating and stripping were performed on Li‖Cu cells, where Cu serves as the working electrode and Li foil serves as the counter electrode. The Li was deposited on Cu at various current densities with a capacity of 1 mAh/cm^2. The deposited Li was then fully stripped to a cutoff voltage of 1 V. The Coulombic efficiency was defined as the amount of stripped Li divided by the amount of plated Li, and the average Coloumbic efficiency was calculated from this result for a range of current densities; the error bars denote the minimum and maximum measured values.

$LiFePO_4$ was used as the cathode while Li metal served as the counter electrode in full cells tested using standard galvanostatics. The charge and discharge currents were calculated based on the electrode size. For the baseline cell, the SAW device was present but was left off throughout testing. For the SAW-driven cell, the SAW device was turned on upon detection of the charging of the cell and was turned off during discharge. The charge-discharge cycling and the associated operation of the SAW device were automated during the experiments (LabVIEW), with a signal generator (SG–380, Stanford Research Systems) and amplifier (ZHL–1–2W, Mini-Circuits) used to drive the SAW device.

Morphological characterization

The cycled batteries were disassembled inside an argon-filled glovebox, the electrodes were collected, and the electrode samples were rinsed with dimethyl carbonate (Sigma-Aldrich) to remove the residual electrolyte on the surface of the electrode. The samples were then attached to a specimen holder (Ted Pella) using double-side carbon tape (Ted Pella) and sealed within an aluminized polyethylene bag inside the glovebox for transferring samples to the SEM. After transport to the SEM, the samples were quickly transferred from the bag to the scanning electron microscopy vacuum chamber (SEM Quanta 250, FEI Corp.) for imaging at 5 kV. The samples were exposed to air for less than three seconds.

Supplementary Information

Mitigating corrosion of the SAW devices by the electrolyte

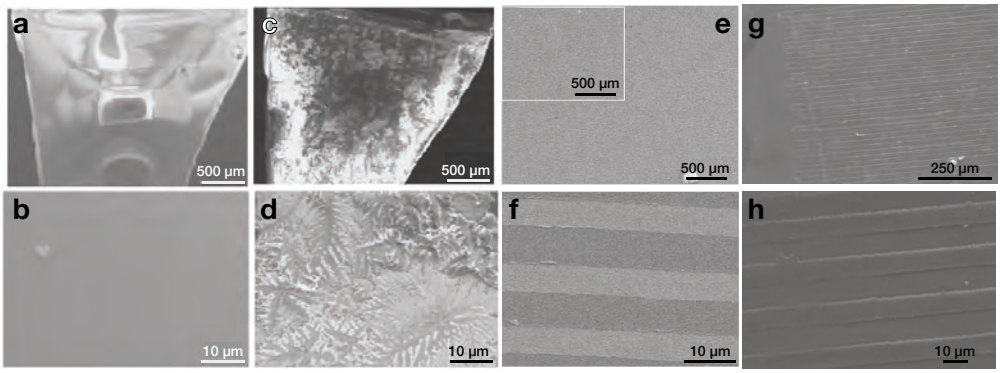

Figure S1: **Preventing SAW device corrosion from the 1M $LiPF_6$ EC/DEC electrolyte by parylene coating.** The **a** pristine LN exhibits a **b** smooth surface morphology that, after seven days' exposure to the electrolyte is corrosively roughened **c** visibly and **d** at the microscale. By coating the SAW device with 200 nm parylene, after two months' exposure to the electrolyte there is no apparent **e** visible or **f** microscale corrosion damage of the LN or the Al SAW IDT fingers: note the fingers are visible as dark stripes in the latter image. Likewise, testing the parylene-coated SAW device in a battery for 280 cycles shows no **e** visible or **f** microscale damage; the IDT Al fingers are visible in both images in this test.

Scanning electron microscope (SEM) images (Fig. S1) indicate the condition of the LN substrate immersed in 1M $LiPF_6$ EC/DEC electrolyte. The pristine morphology of the optically polished LN surface (Fig. S1a,b) is corroded (Fig. S1c,d) by only seven days' immersion in the electrolyte, with 100-μm long fractal tree-like structures across the surface. Since the EC/DEC electrolyte corrodes the unprotected LN substrate, a thin, electrochemically compatible, durable, and acoustically-compatible material is required to protect the SAW device.

Parylene was selected,[36] and we first determined the effects of its deposition on the device's SAW displacement, velocity, and acceleration—which are exquisitely sensitive to surface contaminants or coatings—by measuring them using laser Doppler vibrometry (UHF–120–SV, Polytec, Waldbronn, Germany). The effect of the 200 nm parylene coating itself is weak, with a $< 1\%$ decrease in the displacement, velocity, and acceleration from the uncoated SAW device. The parylene film further appears to be stable in the harsh environment of the electrolyte and ef-

Table 1: **Parylene protects the SAW device from electrolyte corrosion with minimal impact on SAW performance.** The performance of the SAW device without parylene and immediately after immersion is described in terms of the surface displacement, particle velocity, and acceleration. These results remain within 2% of the original after coating with parylene and reimmersing the SAW device in the electrolyte, and after operating the SAW device with parylene in electrolyte to operate the SAW Li‖LMB over 280 charge-discharge cycles (at 1 C).

	Uncoated SAW	Parylene-coated SAW	Parylene-coated SAW after 280 cycles in electrolyte
Displacement (pm)	4.826	4.762	4.714
Velocity (mm/s)	4.069	4.01	3.97
Acceleration (Mm/s^2)	1.952	1.931	1.92

fectively protects the SAW device when immersed for two months in the electrolyte (Fig. S1e,f). This protection extends to actual use of the SAW device in batteries, as confirmed from the morphological evidence in Fig. S1g,h and the vibration characteristics of the SAW device reported in Table S1 after using it in 280 charge-discharge cycles of the SAW Li‖LFP battery.

Prototype Li metal battery configuration.

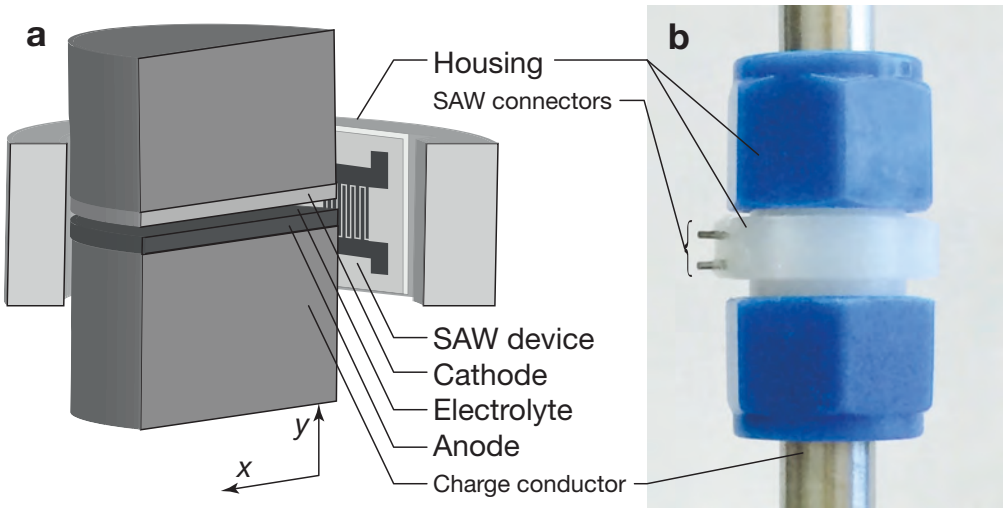

Figure S2: **Prototype Li metal battery configuration.** A **a** schematic cutaway and a **b** photo of an assembled prototype LMB, showing the placement of the SAW device to drive electrolyte recirculation. For scale, the charge conductors are 16 mm in diameter and the gap between the Li anode and $LiFePO_4$ cathode is 25 μm.

First cycle Li deposition onto Cu electrode

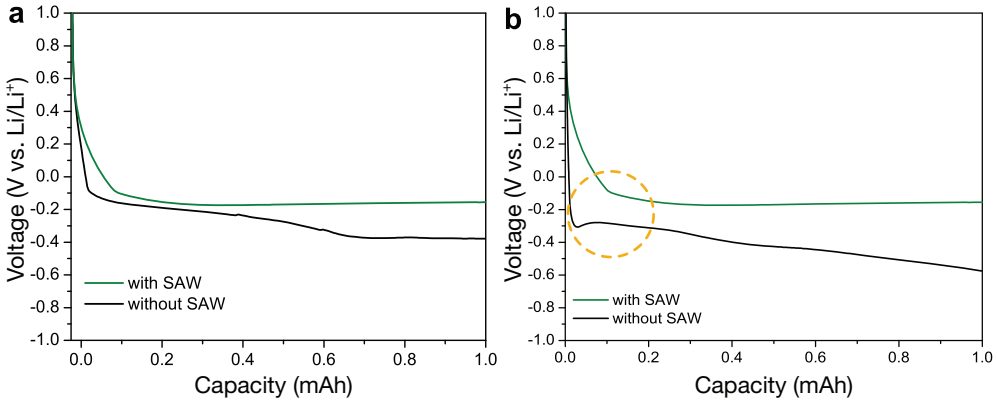

Figure S3: **First cycle deposition voltage profile of Li‖Cu batteries with and without SAW at 1 and 6 mA/cm^2 deposition rates to capacity of 1 mAh/cm^2. a,** comparison of the electrodeposition curves at deposition rate of 1 mA/cm^2 with (green) and without (black) SAW. **b,** comparison of the electrodeposition curves at 6 mA/cm^2 current densities with (green) and without (black) SAW.

Li deposition upon Cu electrode at different SAW power inputs

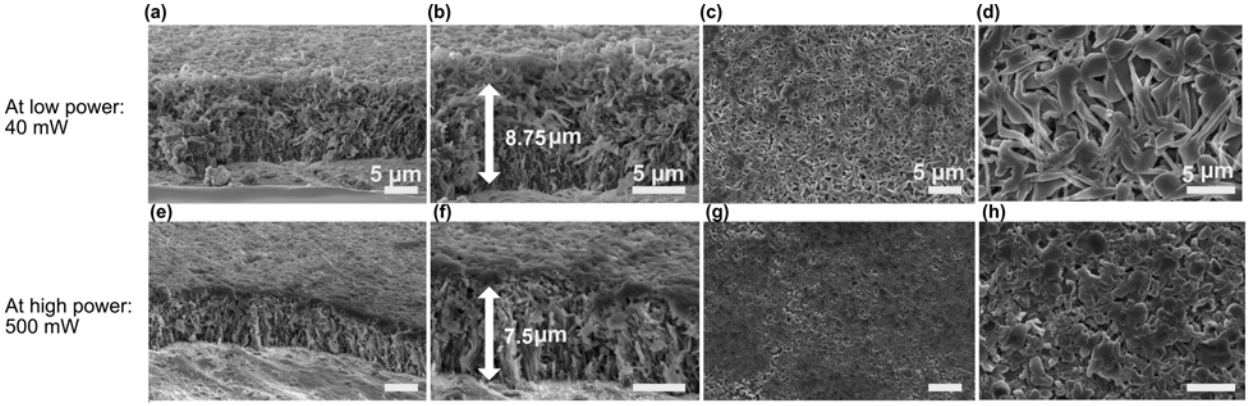

Figure S4: **Li deposition upon a Cu electrode at 6 mA/cm^2 to a capacity of 1 mAh/cm^2** is affected by using different SAW input powers of (a-d) 40 mW and (e-h) 500 mW. Compare these results to those reported in Fig. 2 with a SAW input power of 100 mW and the baseline cells without any SAW at all.

A closer view of the Li deposition upon the Li anode

Higher resolution images of the Li anode after cycling without SAW (*main text* Fig. 3h) and with SAW (*main text* Fig. 3j) are shown, respectively in Fig. S5(a,b) and Fig. S5(c,d). The differences

in the morphology of uncycled Li and cycled Li are more easily seen in these images: the uncycled Li shows a dense and layered structure, while the cycled Li shows a porous structure. This characteristic Li morphology can likewise be seen in past literature.[37]

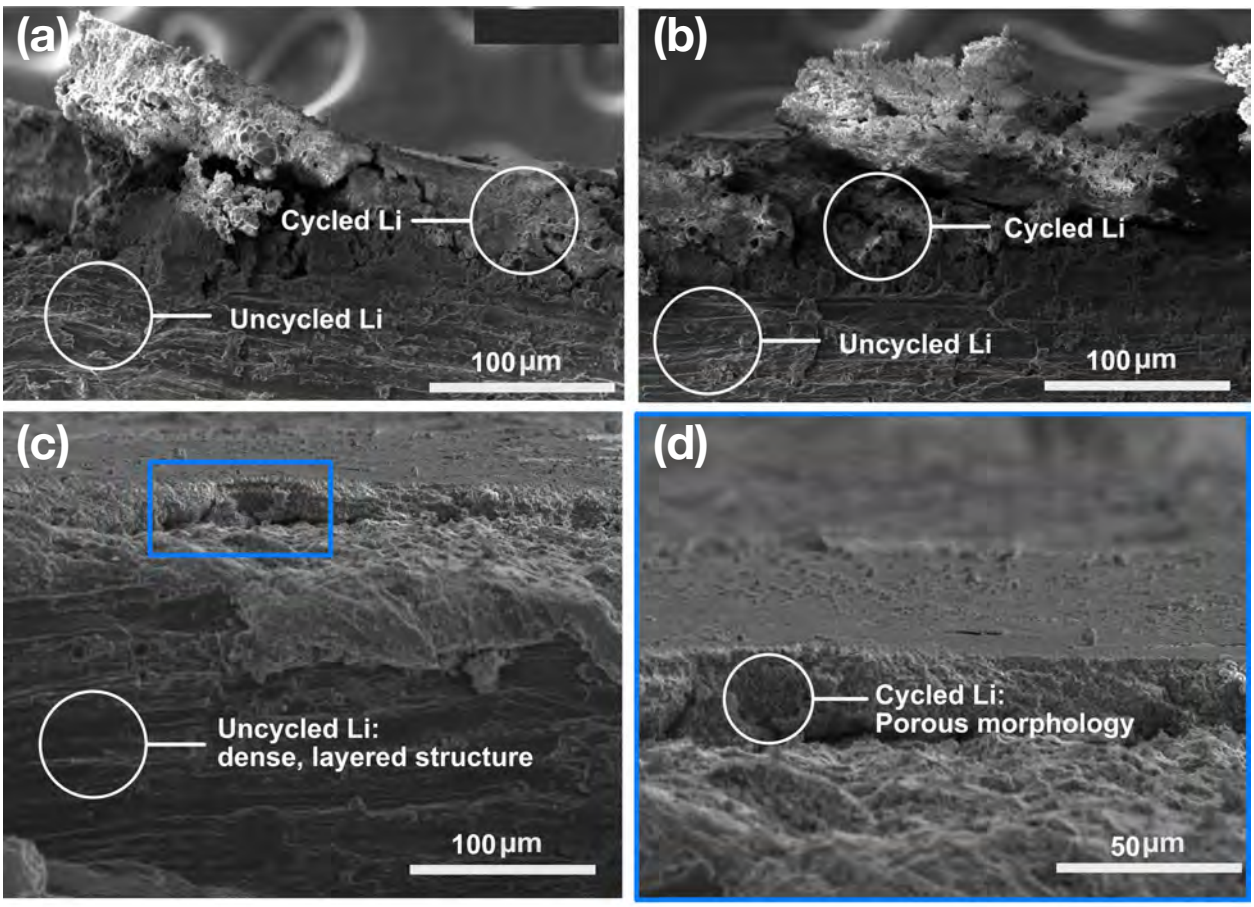

Figure S5: **Cross-sectional SEM images of the Li anode from a SAW LMB, zoomed in to detail the morphology in comparison to Fig. 3.** Without SAW, the cycled Li appears porous in comparison to the dense, layered morphology of the uncycled Li in (a,b) two different locations on the Li anode. With SAW, the (c) Li morphology of the anode is somewhat more difficult to see, though (d) zooming in further shows a clear difference between the modestly porous cycled Li and the dense, layered uncycled Li.

Initial roughness of the Li anode to determine λ — the distance between "hotspots"

The presumption of a sinusoidal morphology for the Li electrode in the closed-form analysis briefly described in the main text and provided in detail later in this Supplementary Information is a method to overcome the extraordinary difficulty of the computations necessary to pro-

duce useful results for the electrochemistry with electrolyte flow, to produce useful closed-form results as a design tool for incorporating SAW into batteries, and in recognition of the fact that pristine, as-supplied Li metal is rough and often has an observably dominant length scale as shown in Fig. S6: $\lambda \approx 200\mu$m.

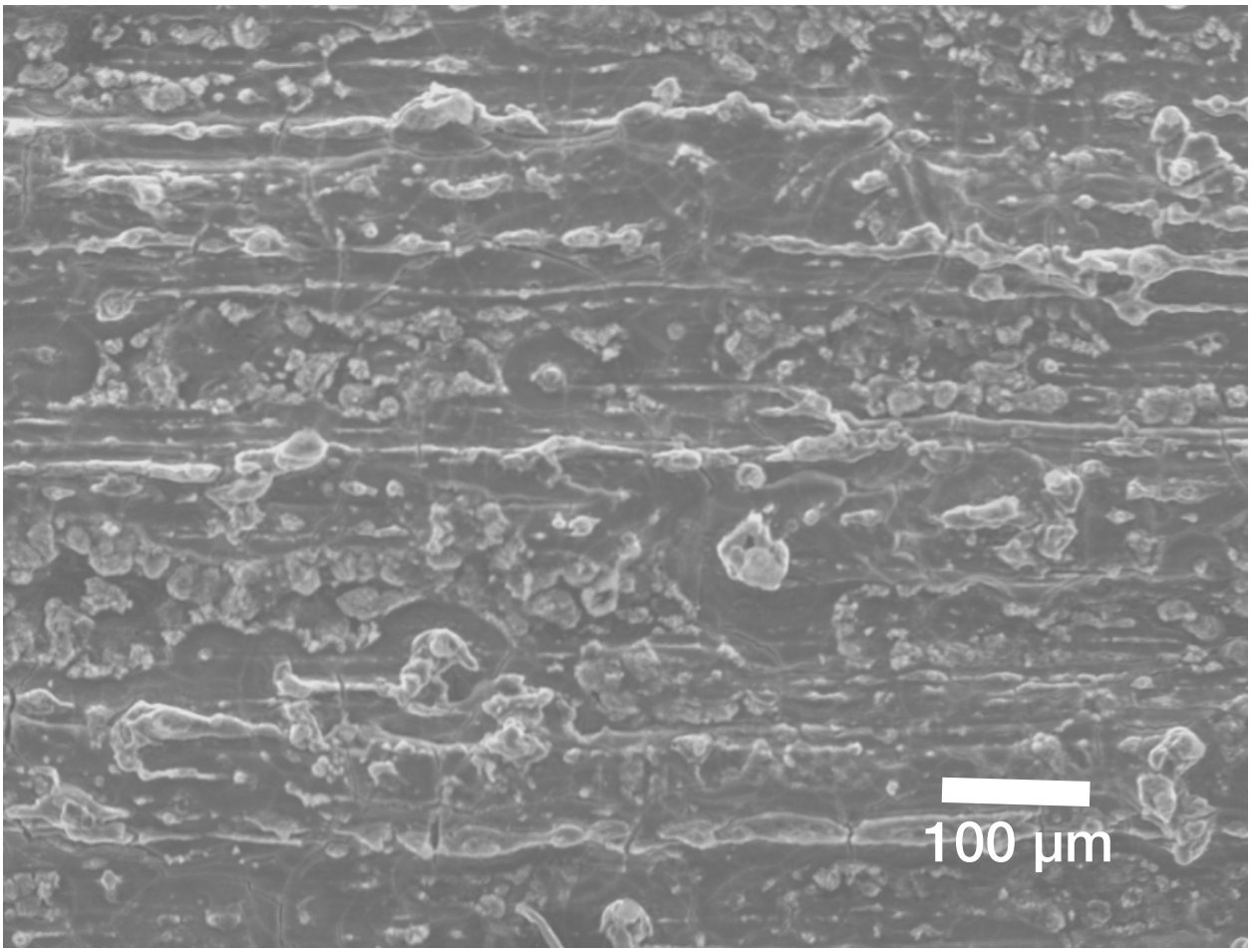

Figure S6: **SEM image of pristine Li anode prior to use in battery.** The surface of the Li has machining marks with a characteristic length scale to suggest $\lambda = 200\mu$m for our analysis in predicting the necessary SAW-driven acoustic streaming flow required to avoid dendrite formation and porous Li deposition.

Examination of the flow mechanism acting to suppress nonuniform Li deposition

The representation of electrolyte flow and ion transport

The steady mass transport of ions, assuming the electrical field in the battery is effectively screened by the high electrolyte concentration, is governed by

$$\mathbf{u} \cdot \nabla c = D \nabla^2 c, \tag{2}$$

where $c, \mathbf{u}, D$ are the ion concentration, velocity field, and the constant ion diffusion coefficient, respectively. To simplify the problem we further assume a 2D problem, in which the x coordinate is along the flow in the boundary layer and the y coordinate traverses the electrodes, which are assumed to be flat and parallel (prior to the physical growth of dendrites). We solve the problem subject to the mass conservation of metal ions in the electrolyte[30] and a harmonic variation in ion concentration along the surface of the Li electrode, which is associated with local ion depletion areas in the vicinity of hotspots for the growth of dendrites,

$$\frac{1}{A} \int \int_A c \, dA = c_{\text{bulk}} \tag{3}$$

and

$$c = \epsilon c_{\text{bulk}} \left(1 + \cos(kx)\right) \text{ at } y = 0, \tag{4}$$

respectively, where A is the area between the electrodes along the x and y coordinates in a 2D view of the system, c_{bulk} is the concentration of Li ions in the electrolyte, ϵ is a small perturbation parameter of the excess ion depletion near hotspots with compare to the level of ion depletion away from hotspots, and k is a perturbation wavenumber of ion depletion, which physically may be taken to account for the density of the hotspots along the Li electrode with a corresponding wavelength of $2\pi/k$ that is associated with the characteristic separation be-

tween hotspots. Here, it also is associated with the physical roughness of the pristine Li anodes in Fig. S6. The surface of the Li electrode is given at $y = 0$. In these expressions, localized minima along the Li electrodes are permitted, where the ion concentration fully vanishes and hence supports the hotspots. The velocity field in the boundary layer is taken to be $u = \beta y e_x$ and $v = 0 e_y$, where u and v are the components of the velocity field along the e^x and e^y unit vector directions associated with the x and y coordinates, respectively, and $\beta \approx u_c/\delta$ is the shear rate along the y coordinate, where δ is a characteristic length of the flow in the boundary layer. The current carried in large part by the ions is a function of the electrical potential difference between the electrodes.[38,39]

Experimental examination of the interelectrode electrolyte flow induced by the SAW device

The presumption of steady shear flow was made based on the experimental observation of the interelectrode flow in a transparent "dummy" battery where the solid components were replaced by acrylic and the electrolyte was replaced by deionized water laden with 200-nm fluorescent polystyrene nanoparticles (Fluoresbrite YG 0.20 μm, Polysciences, Warrington, PA USA) at a concentration of 10^5 particles/mℓ. The particle size was chosen[16] to be smaller than the threshold at which direct acoustic forces can impart a significant force upon them, and so the particles moved via viscous drag to indicate the fluid flow. A simplified form of submicron particle image velocimetry was then conducted, recording the particle motion at 5000 fps and 12,000 ISO via high-speed camera (FASTCAM Mini, Photron, San Diego, CA USA) imaging through a long-working distance microscope (K2 DistaMax, Infinity Photo-Optical, Centennial, CO USA) and bandpass filter for the 532-nm light emission from the particles (86–355 filter, Edmund Optics, Barrington, NJ USA) while being illuminated with a 139 lumen white light (NL660, Neewer, Edison, NJ USA). The captured high-speed videos were processed[40] to produce velocity field information (Particle image velocimetry tool, MATLAB R2019a, MathWorks, Natick, MA USA) as shown, for example, in Fig. S7. Other regions of the interelectrode gap exhibit similar flow profiles.

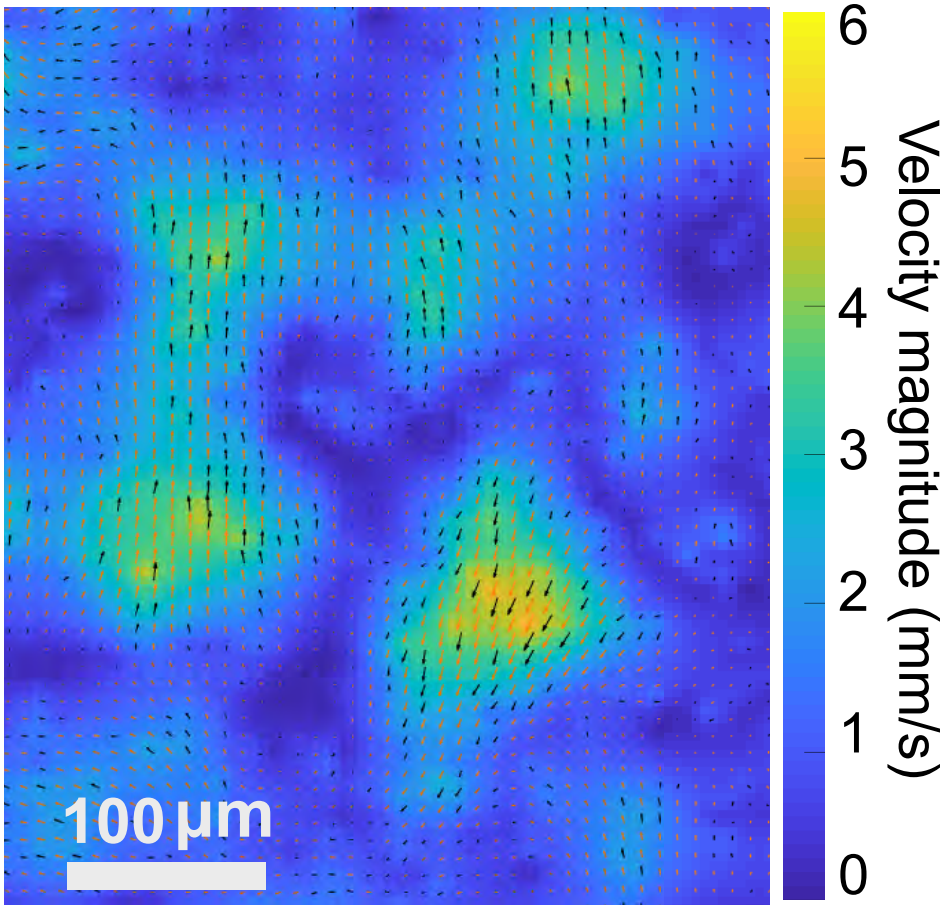

Figure S7: **Fluid flow distribution in the 50 μm interelectrode gap due to SAW from particle image velocimetry.** The fluid velocity is plotted in a 500μm×500μm region showing weak vortices but otherwise uniform flow driven by the SAW device at 474 mW and 100 MHz. The flow is steady and otherwise unremarkable. Particle image velocimetry-derived fluid velocity while the SAW device is being operated at 474 mW. The mean fluid velocity is 5 mm/s. The arrows indicate the flow direction.

The resulting flow shown in Fig. S7 is weakly vortical with an average velocity of 5 mm/s for 100 MHz SAW at 474 mW from a SAW device with a 10 mm aperture and interelectrode gap of 50 μm, in agreement with substantial past evidence of similar acoustic streaming velocities in microdevices,[14] and the thickness of each electrolyte chamber in the battery, i.e., $L = 50$ μm, as a characteristic length. No turbulence, unsteady flow, or otherwise atypical flow was observed supporting the contention that a simple shear flow model for the electrolyte is suitable.

Simulation of the SAW-driven interelectrode gap electrolyte flow, ion transport, and anodic ion deposition

To further validate this result, two-dimensional computational analysis (COMSOL Multiphysics 5.3a, COMSOL Corp., Stockholm, Sweden) was used to determine the Li^+ ion concentration gradient in the electrolyte in an LMB with diffusion and either with or without SAW-driven acoustic streaming. The charge transport via deposition of Li^+ ions upon the anode during charging was also included to examine the effects of removing the Li^+ ions from the electrolyte.

For the LMB absent SAW, the electrochemistry module was used with a physics-controlled mesh, tertiary current distribution, and the Nernst-Planck interface. This interface describes the current and potential distribution in an electrochemical cell, taking into account the individual transport of the Li^+ ions and uncharged species alike in the electrolyte due to diffusion, migration, and convection using the Nernst-Planck equation,

$$\frac{\partial c_i}{\partial t} + \bigtriangledown \cdot N_i = R_i, \tag{5}$$

where N_i is the flux of charged species in the electrolyte and can be expressed as: $N_i = -D_i \bigtriangledown C_i - z_i u_m F_{ci} \bigtriangledown V + C_i u$, where C_i is the concentration of ions i, z_i is the charge transfer number, D_i is the diffusion coefficient, u_m is the mobility, F is the Faraday constant, V is the battery potential, and u is the velocity vector.

In the SAW-driven LMB, the simulation is more complex, necessitating the sequential use

of the pressure acoustic, creeping flow, and electrochemistry modules for frequency and time-domain computations. Because acoustic streaming depends upon the existence of viscosity and compressibility in fluid flow, the typical assumptions of incompressible Stokesian flow at small scales is inappropriate. Instead we must resort to using the full Navier-Stokes representation in conservation of momentum.[18] Through knowledge of the amplitude distribution of the SAW acoustic source in our representative setup using laser Doppler vibrometry (UHF–120–SV, Polytec, Waldbronn, Germany), we may define a velocity boundary condition at the electrolyte boundary adjacent the SAW device with attenuation of the SAW in the substrate defined by the length scale α,[35] that is dependent upon the characteristics of the fluid and the SAW. The "pressure acoustic" module in COMSOL provides a means to determine the distribution of the nonlinear acoustic wave in the fluid, permitting finite amplitude acoustic wave propagation such as might be present here from the use of very high frequency acoustic (fast) waves.[18] The attenuation of these acoustic waves in the fluid gives rise to a momentum flux (Reynolds stress) and in turn a net body force imposed upon the fluid. In the context of COMSOL-based computations, the body force may be directly computed from a spatial gradient of the wave's potential energy, and this body force may then be transferred to another module in COMSOL, the "creeping flow" module designed to produce laminar flow from an imposed body force distribution as a time-averaged representation of the conservation of mass and momentum.

The electrochemistry module is then used in COMSOL to determine the ion concentration gradient in the electrolyte in conjunction with the convection-diffusion equation representing the Li^+ ion species present in the electrolyte, its deposition upon the anode, and its extraction from the cathode.

The dimensions and properties of the Li‖LFP cell were used with charge rates of 6 mA/cm^2 (equivalent to 6 C) to produce the results shown in in Fig. 1b,c—for flow field and Li^+ ion concentration with distorted spatial scale for ease of visualization, and Fig. S8—where the Li^+ ion concentration gradient is illustrated at different states of charge.

The analysis lacks any initial "hotspots" as posited to exist in the forthcoming closed-form

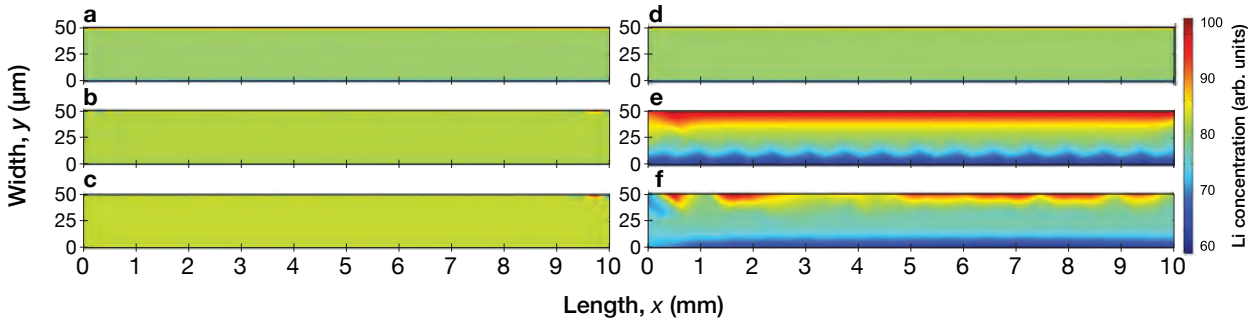

Figure S8: **Change in the Li^+ concentration gradient for both a SAW and baseline Li‖LFP at different states of charge (SOC).** With SAW-driven acoustic streaming, the Li^+ concentration in the interelectrode gap is homogeneous at **a,** 0%, **b,** 50%, and **c,** 100% SOC. Without SAW, the baseline Li‖LFP cell develops significant concentration gradients from **d,** 0% to **d,** 50% and **e,** 100% SOC.

analysis, but does nonetheless indicate the benefit of SAW-driven acoustic streaming flow in reducing the inhomogeneous Li^+ ion distribution in the interelectrode gap. For both versions of the Li‖LFP cell, with and without SAW, the Li^+ ion concentration in the electrolyte is initially homogeneous. However, as charging progresses, the Li^+ ion concentration becomes inhomogeneous in the baseline cell, while in the SAW cell it remains homogeneous. The computational analysis is useful for a qualitative assessment of the observed phenomena. However, the phenomena is better explored by experiment and theory due to the computational cost of such high-frequency multidisciplinary physics, especially with the relatively slow COMSOL platform.

Most importantly, as with the μPIV experiment, the results of the COMSOL analysis supports the contention that SAW acoustic-streaming generated steady shear flow is sufficient to produce reductions in Li^+ ion gradients and improvements in Li^+ ion plating during charging. Mixing flow, turbulence, or otherwise unsteady flow phenomena are unnecessary.

With these results in mind, we next seek to devise a theoretical model to represent the system.

A route to a closed-form model for the SAW-driven LMB Li^+ ion diffusion and deposition phenomena

Using the transformations $x \to \delta x,\ y \to \delta y,\ c \to c_{\text{bulk}} c,\ (u,v) \to u_c(u,v),\ L \to \delta L,\ k \to k\delta, h \to h/\delta$ we render the problem in eqns. (2), (3), and (4) dimensionless, giving,

$$u\partial_x c + v\partial_y c = \frac{1}{\text{Pe}}\left(\partial_{xx} c + \partial_{yy} c\right), \tag{6}$$

with the Peclet number defined as Pe=u_c/D; eqn. (6) is subject to

$$\frac{1}{A}\int\int_A c\, dA = 1 \tag{7}$$

$$c = \epsilon\,(1+\cos(kx)) \text{ at } y = 0, \tag{8}$$

where we encounter two small parameters in this problem, i.e., $1/\text{Pe} \ll 1$ ($\text{Pe} = u_c\delta/D \gg 1$) in eqn. (6) and $\epsilon \ll 1$ in eqn. (8). We assume a simple shear flow in the vicinity of the Li electrode, so that $u = y$ and $v = 0$.

The system of equations (6)–(8) supports a transport boundary layer of ions and hence is associated with a singular asymptotic expansion of the concentration c in $1/\text{Pe}$. We thus consider an outer concentration field far from the Li electrode, described by C, and an inner (boundary layer) concentration field near the electrode, described by c. In order to solve the inner (boundary layer) problem we rescale the coordinate y in the form $y = Y\text{Pe}^{-n}$, so that the leading order diffusive term satisfies convection. Both concentration fields must satisfy $\lim_{y\to 0} C = \lim_{Y\to\infty} c$. We then expand the leading order concentration field in powers of ϵ according to the series expansion $C = C_0 + \epsilon C_1 + \ldots$ and $c = c_0 + \epsilon c_1 + \ldots$ as follows.

Leading order ($O(1)$) expansion To leading order, the problem in eqns. (6)-(8) in the outer field satisfies the system of equations

$$u\partial_x C_0 + v\partial_y C_0 = 0,$$

and

$$\frac{1}{A}\int\int_A C_0\, dA = 1,$$

which gives the trivial solution $C_0 = 1$. In the inner (boundary layer) field, where we use the transformation $y = Y\mathrm{Pe}^{-n}$, the problem takes the leading order form,

$$Y\partial_x c_0 = \partial_{YY} C_0,$$

where $n = 1/3$, so that the leading order diffusive terms is satisfied by convection. The corresponding boundary conditions at the surface of the electrode and far away from the boundary layer (where the inner solution is matched to the outer solution) are then,

$$c_0 = 0 \text{ at } Y = 0, \quad \text{and} \quad c_0 = 1 \text{ at } Y \to \infty,$$

respectively. An analytical similarity solution to this problem is obtained by using the transformation $\zeta \equiv Y/x^{1/3}$. The boundary layer problem translates then to,

$$-\frac{\zeta^2}{3}\frac{dc_0}{d\zeta} = \frac{d^2 c_0}{d\zeta^2},$$

and

$$c_0 = 0 \text{ at } \zeta = 0, \;\; c_0 = 1 \text{ at } \zeta \to \infty.$$

This system of equations is satisfied by

$$c_0 = \frac{3^{1/3}}{\Gamma(1/3)}\int_{\zeta'=0}^{\zeta} e^{-\zeta'^3/9} d\zeta', \tag{9}$$

where $\Gamma()$ is the Euler gamma function and $\Gamma(1/3) \approx 2.68$. Taking the y derivative of the leading order concentration near the surface of the Li electrode at $Y = \zeta = 0$ gives

$$\partial_y c_0|_{y=0} = \frac{dc_0}{d\zeta} \times \partial_y \zeta|_{y=\zeta=0} = \frac{3^{1/3}}{\Gamma(1/3)}\left(\frac{\mathrm{Pe}}{x}\right)^{1/3}. \tag{10}$$

Hence the dimensional flux of ions to the electrode is,

$$i_0 = -D\partial_y c_0|_{y=0} = -D\frac{3^{1/3}}{\Gamma(1/3)}\frac{c_{\text{bulk}}}{\delta}\left(\frac{\text{Pe}}{x/\delta}\right)^{1/3}, \tag{11}$$

where the negative sign infers that the flux is to the electrode. Thus, it is clear that the current generally increases when the Peclet number (the convective flow) increases and when the characteristic length scale of the flow decreases (shear rate increases) while the surface of the electrode is flat and homogeneous. Moreover, the current decreases downstream since the convection of ions reduce the variations in ion concentration along this direction.

Second order ($\mathcal{O}[\epsilon]$) expansion Since C_0 is a constant, the next-order problem in eqns. (6)–(8) in the outer field satisfies the system of equations

$$u\partial_x C_1 + v\partial_y C_1 = 0,$$

$$\frac{1}{A}\int\int_A C_1 \, dA = 0,$$

which, again, gives the trivial solution $C_1 = 0$.

The next-order problem in eqns. (6)–(8) in the inner field is

$$Y\partial_x c_1 = \partial_{YY} c_1 + \partial_{xx} c_0, \tag{12}$$

$$c_1 = 1 + \cos(kx) \text{ at } Y = 0, \tag{13}$$

$$c_1 = 0 \text{ at } Y \to \infty, \tag{14}$$

where again we use the transformation $y = Y\text{Pe}^{-1/3}$ and further require that $\epsilon \approx \text{Pe}^{-2/3}$ in order to include the perturbation of the ion concentration in eqn. (13). This problem may be written as a superposition of three subproblems, where $c_1 = c_{1,1} + c_{1,2} + c_{1,3}$. Solving the problem for $c_{1,1}$, which is given by omitting the forcing term $\partial_{xx} c_0$ from eqn. (12) and replacing eqn. (13) by

$c_{1,1} = 1$ at $Y = 0$, one finds

$$c_{1,1} = -\frac{3^{1/3}}{\Gamma(1/3)} \int_{\zeta'=0}^{\zeta} e^{-\zeta'^3/9} d\zeta'. \tag{15}$$

Hence, the corresponding dimensional flux of ions is

$$i_{1,1} = -D\partial_y c_{1,1}|_{y=0} = D\frac{3^{1/3}}{\Gamma(1/3)} \frac{c_{\text{bulk}}}{\delta} \left(\frac{\text{Pe}}{x/\delta}\right)^{1/3}. \tag{16}$$

One can further write the problem for $c_{1,2}$ by omitting the forcing term $\partial_{xx} c_0$ from eqn. (12) and replacing eqn. (13) by $c_{1,2} = \cos kx$ at $Y = 0$. The problem is written as

$$Y\partial_x \tilde{c}_{1,2} = \partial_{YY} \tilde{c}_{1,2}, \tag{17}$$

$$\tilde{c}_{1,2} = e^{ikx} \text{ at } Y = 0, \tag{18}$$

and

$$\tilde{c}_{1,2} = 0 \text{ at } Y \to \infty. \tag{19}$$

using the complex variable $\tilde{c}_{1,2}$ whose real component is $c_{1,2}$. Using the transformation $\tilde{c}_{1,2} = f(Y)e^{ikx}$ in eqns. (17)–(19) produces the alternate system of equations

$$ikYf = \frac{d^2 f}{dY^2},$$

$$f = 1 \text{ at } Y = 0,$$

and

$$f = 0 \text{ at } Y \to \infty,$$

which is satisfied by the complex solution

$$f = 3^{2/3}\Gamma(2/3)\text{Ai}\left((ik)^{1/3}Y\right), \tag{20}$$

where Ai is the Airy function of the first kind. The Airy function decays in the limit $Y \to \infty$ subject to the argument $(ik)^{1/3}$. The real component of the Y derivative of $\tilde{c}_{1,2}$ is given by

$$\partial_Y c_{1,2}|_{Y=0} = \frac{\sqrt{\pi}(3/2)^{1/3}}{\Gamma(1/6)} k^{1/3} \left(\sin(kx) - \sqrt{3}\cos(kx)\right). \tag{21}$$

Hence, the corresponding dimensional flux of ions is,

$$\begin{aligned} &i_{1,2} = -D\partial_y c_{1,2}|_{y=0} = \\ &-D\frac{\sqrt{\pi}(3/2)^{1/3}}{\Gamma(1/6)} \frac{c_{\text{bulk}}}{\delta} (k\delta)^{1/3} \left(\sin(kx) - \sqrt{3}\cos(kx)\right) \text{Pe}^{1/3}. \end{aligned} \tag{22}$$

Finally, one can write the problem for $c_{1,3}$ using eqn. (12) and replacing eqn. (13) by $c_{1,3} = 0$ at $Y = 0$. The problem for $c_{1,3}$ gives a spatially monotonic solution and requires a numerical solution; however, this solution does not contribute to the leading order solution for the dendrite-free region of the electrode denoted by x_{crit}. Hence, we refer to the solution of this problem on the order of magnitude of $\mathcal{O}[\epsilon]$ as follows.

The total ion flux to the Li electrode is given by $i = i_0 + \epsilon(i_{1,1} + i_{1,2} + i_{1,3})$, which translates to

$$\begin{aligned} &\frac{-i}{\text{Pe}^{1/3} D c_{\text{bulk}}/\delta} = \frac{3^{1/3}(1-\epsilon)}{\Gamma(1/3)} (x/\delta)^{-1/3} + \\ &\epsilon\frac{\sqrt{\pi}(3/2)^{1/3}}{\Gamma(1/6)} (k\delta)^{1/3} \left(\sin(kx) - \sqrt{3}\cos(kx)\right) + \mathcal{O}[\epsilon], \end{aligned} \tag{23}$$

where we note again that $\epsilon \approx \text{Pe}^{-2/3}$. We further highlight that a similar problem and solution appear when where the value of ϵ is arbitrary while satisfying $1 \gg \epsilon \gg Pe^{-2/3}$, with the exception that the forcing term $\partial_{xx} c_0$ does not exist in eqn. (12), and hence the result given in eqn. (23) does not contain the third term on the right hand side of the equation, given as $\mathcal{O}[\epsilon]$.

Li^+ ion gradient within stationary electrolyte: $\beta = 0$

In the absence of flow, we find that the diffusion-limited flux of ions to the electrode, $-i$, is given by,

$$-i = D\left(\frac{2c_{\text{bulk}}(1-\epsilon)}{L} - \epsilon c_{\text{bulk}} k\cos(kx)\right), \tag{24}$$

where the negative sign in front of i appears because the flux of ions to the electrode is along the $-y$ axis direction. The flux of ions is locally enhanced near the hotspots, suggesting the initial Li^+ ion concentration gradient and subsequent nonuniform Li^+ plating and dendrite growth is inevitable.

The effect of electrolyte flow, $\beta > 0$, on the Li^+ ion gradient

The presence of flow near the Li electrode enhances the advection of Li ions to the electrode in a manner proportional to $\text{Pe}^{1/3}$, where $\text{Pe} \equiv u_c l/D$ is the Peclet number.[34] In addition, we show that the flow further enhances the local transport of Li ions to the hotspots in a manner proportional to $\text{Pe}^{1/3}$. This result is expected since the enhanced convection of ions along the electrode to the hotspots decreases variations in ion concentration that would otherwise arise. The overall rate of Li ion adsorption onto the electrode is given by

$$\frac{-i}{\text{Pe}^{1/3} D c_{\text{bulk}}/\delta} = \frac{3^{1/3}(1-\epsilon)}{\Gamma(1/3)}\left(\frac{x}{\delta}\right)^{-1/3} + \epsilon\frac{\sqrt{\pi}(3/2)^{1/3}}{\Gamma(1/6)}(k\delta)^{1/3}\left(\sin(kx) - \sqrt{3}\cos(kx)\right) + \mathcal{O}[\epsilon], \tag{25}$$

where we assume that $\epsilon \approx \text{Pe}^{-2/3}$ (albeit similar result appears when requiring that $1 \gg \epsilon \gg \text{Pe}^{-2/3}$), and note that $\Gamma(1/3) \approx 2.68$ and $\Gamma(1/6) \approx 5.57$. The first term on the right indicates the spatially monotonic convective contribution of ion flux to a flat homogeneous electrode and the second term indicates the correction to the spatially non-monotonic convective ion flux due to the presence of the hotspots. The third term given simply as $\mathcal{O}[\epsilon]$ is an additional convective contribution to the ion flux, which is spatially monotonic and may be obtained numerically. We note that the first and third terms are products of similarity analysis and hence are mathematically singular at the origin, $x = 0$, and hence the expression for the current in eqn. (25) is

physically valid far from the origin.

The mechanism by which flow inhibits the growth of dendrites is counterintuitive. The flow enhances the flux of Li^+ ions to the electrode and particularly to the hotspots where dendrites may grow, as given independently by the first and second terms on the right side of eqn. (25), respectively. The ion flux is spatially perturbed by ion depletion next to hotspots for the growth of dendrites, which is given in the second term in the equation. However, the leading order convection term, which decays like $x^{-1/3}$ along the electrode, eliminates localized ion flux maxima and hence is the key to the inhibition of dendrites' growth. The combined contribution of both terms eliminates localized ion transport maxima to the electrode and hence eliminates spatially localized growth spots— dendrites—on the electrode. But this suppression of dendrite growth is only over a finite length of the electrode from $x = 0$, where the shear flow (or alternatively the electrode) commences, to $x < x_{\text{crit}}$; as x grows, the second of the two terms in eqn. (25) becomes dominant and the hotspots at $x \geq x_{\text{crit}}$ will begin to allow dendrite growth. To determine this critical length, we require the slope of ion flux to not change sign with respect to x along the electrode, such that $d(-i)/dx < 0$, thus avoiding localized ion flux maxima along the electrode. Substituting eqn. (25) into the non-equality, replacing the spatial derivative of the term $\sin(kx) - \sqrt{3}\cos(kx)$ by its numerical upper bound, 2, and ignoring the second order ($\mathcal{O}[\epsilon]$) spatially monotonic contributions to ion flux along the electrode surface, thus comparing between the contribution of the leading order spatially monotonic ion flux and the leading order (harmonic) contribution to the ion flux from the presence of dendrites, gives

$$x_{\text{crit}} = \left(\frac{6\epsilon k^{4/3}\beta}{\alpha}\right)^{-3/4} \approx 0.35\ k^{-1}\epsilon^{-3/4} \approx 0.35\ k^{-1}Pe^{1/2},$$

where $\alpha \equiv 3^{1/3}(1-\epsilon)/\Gamma(1/3)$ and $\beta \equiv \sqrt{\pi}(3/2)^{1/3}/\Gamma(1/6)$. The correction to the ion flux due to the presence of hotspots in eqn. (25) and in our corresponding estimate of the dendrite free length of the electrode, x_{crit}, are qualitative results. Their quantitative magnitude is given from our requirement that the contribution of ion depletion (next to hotspots) to the ion flux ap-

pears in the first correction (of the order of $\epsilon \approx \mathrm{Pe}^{-2/3}$) to the leading order ($O(1)$) convective result. Hence, x_{crit} indicates that the excitation of flow near the electrode inhibits the growth of dendrites but to a limited electrode length, which is dependent on the properties of the electrode. In particular, x_{crit} increases when reducing the density of hotspots and their intensity, that is, reducing the excess of ion depletion next to the hotspots. Alternatively, it is clear that increasing flow intensity further increases x_{crit}. The curious result here is that this length is independent of the specifics of the flow, but only if the Peclet number is significantly greater than one. Here, our means to ensure the Peclet number is sufficiently large is acoustic streaming, and thus we choose the characteristics of the SAW device and its operation to ensure the amplitude, frequency, and length scale of attenuation of the acoustic wave[35] are appropriately chosen to ensure sufficient flow and avoid nonuniform Li^+ deposition, porosity, and dendrites.

Acknowledgements

This work was performed in part at the San Diego Nanotechnology Infrastructure (SDNI) of UCSD, a member of the National Nanotechnology Coordinated Infrastructure, which is supported by the National Science Foundation (Grant ECCS–1542148). The work presented here was generously supported by a research grant from the W.M. Keck Foundation and the Department of Energy's National Energy Technology Laboratory via grant DE–EE0008363. The authors further acknowledge helpful discussions about the theory with Prof. Nir Gavish, Department of Mathematics, Technion IIT.

References

(1) Liu, J.; Bao, Z.; Cui, Y.; Dufek, E. J.; Goodenough, J. B.; Khalifah, P.; Li, Q.; Liaw, B. Y.; Liu, P.; Manthiram, A. Pathways for practical high-energy long-cycling lithium metal batteries. *Nature Energy* **2019**, *4*, 180–186.

(2) Schmuch, R.; Wagner, R.; Hörpel, G.; Placke, T.; Winter, M. Performance and cost of materials for lithium-based rechargeable automotive batteries. *Nature Energy* **2018**, *3*, 267–278.

(3) Betz, J.; Bieker, G.; Meister, P.; Placke, T.; Winter, M.; Schmuch, R. Theoretical versus practical energy: a plea for more transparency in the energy calculation of different rechargeable battery systems. *Advanced Energy Materials* **2019**, *9*, 1803170.

(4) Zheng, G. W.; Wei, T. Batteries: Just a spoonful of $LiPF_6$. *Nature Energy* **2017**, *2*, 17029.

(5) Goriparti, S.; Miele, E.; De Angelis, F.; Di Fabrizio, E.; Zaccaria, R. P.; Capiglia, C. Review on recent progress of nanostructured anode materials for Li-ion batteries. *Journal of Power Sources* **2014**, *257*, 421–443.

(6) Cheng, X. B.; Zhang, R.; Zhao, C. Z.; Zhang, Q. Toward safe lithium metal anode in rechargeable batteries: a review. *Chemical Reviews* **2017**, *117*, 10403–10473.

(7) Zachman, M. J.; Tu, Z.; Choudhury, S.; Archer, L. A.; Kourkoutis, L. F. Cryo-STEM mapping of solid–liquid interfaces and dendrites in lithium-metal batteries. *Nature* **2018**, *560*, 345–349.

(8) Albertus, P.; Babinec, S.; Litzelman, S.; Newman, A. Status and challenges in enabling the lithium metal electrode for high-energy and low-cost rechargeable batteries. *Nature Energy* **2018**, *3*, 16–21.

(9) Tarascon, J.; Armand, M. Issues and challenges facing rechargeable lithium batteries. *Nature* **2001**, *414*, 359–367.

(10) Lu, Z.; Liang, Q.; Wang, B.; Tao, Y.; Zhao, Y.; Lv, W.; Liu, D.; Zhang, C.; Weng, Z.; Liang, J., et al. Graphitic Carbon Nitride Induced Micro-Electric Field for Dendrite-Free Lithium Metal Anodes. *Advanced Energy Materials* **2019**, *9*, 1803186.

(11) Shen, K.; Wang, Z.; Bi, X.; Ying, Y.; Zhang, D.; Jin, C.; Hou, G.; Cao, H.; Wu, L.; Zheng, G., et al. Magnetic Field–Suppressed Lithium Dendrite Growth for Stable Lithium-Metal Batteries. *Advanced Energy Materials* **2019**, 1900260.

(12) Lai, H. Method for using ultrasound for assisting forming conductive layers on semiconductor devices. 2000; `https://www.google.com/patents/US6159853`, US Patent 6,159,853.

(13) High-density and high-precision printed circuit board copper electroplating process. 2014; `https://www.google.com/patents/CN103806031A?cl=en`, CN Patent App. CN 201,210,444,599.

(14) Connacher, W.; Zhang, N.; Huang, A.; Mei, J.; Zhang, S.; Gopesh, T.; Friend, J. Micro/nano acoustofluidics: materials, phenomena, design, devices, and applications. *Lab on a Chip* **2018**, *18*, 1952–1996.

(15) Li, H.; Friend, J. R.; Yeo, L. Y. Surface acoustic wave concentration of particle and bioparticle suspensions. *Biomedical Microdevices* **2007**, *9*, 647–656.

(16) Shilton, R.; Tan, M. K.; Yeo, L. Y.; Friend, J. R. Particle concentration and mixing in microdrops driven by focused surface acoustic waves. *Journal of Applied Physics* **2008**, *104*, 014910.

(17) Huang, A.; Miansari, M.; Friend, J. Driving useful morphological changes in magnetic nanoparticle structures through the application of acoustic waves and magnetic fields. *Applied Physics Letters* **2018**, *113*, 034103.

(18) Friend, J.; Yeo, L. Y. Microscale acoustofluidics: Microfluidics driven via acoustics and ultrasonics. *Reviews of Modern Physics* **2011**, *83*, 647.

(19) Campbell, C. *Surface Acoustic Wave Devices for Mobile and Wireless Communications*; Academic Press, Inc., 1998.

(20) Zhang, X. Q.; Cheng, X. B.; Chen, X.; Yan, C.; Zhang, Q. Fluoroethylene carbonate additives to render uniform Li deposits in lithium metal batteries. *Advanced Functional Materials* **2017**, *27*, 1605989.

(21) Yan, C.; Cheng, X.-B.; Tian, Y.; Chen, X.; Zhang, X.-Q.; Li, W.-J.; Huang, J.-Q.; Zhang, Q. Dual-layered film protected lithium metal anode to enable dendrite-free lithium deposition. *Advanced Materials* **2018**, *30*, 1707629.

(22) Zheng, J.; Engelhard, M. H.; Mei, D.; Jiao, S.; Polzin, B. J.; Zhang, J.-G.; Xu, W. Electrolyte additive enabled fast charging and stable cycling lithium metal batteries. *Nature Energy* **2017**, *2*, 17012.

(23) Liu, Y.; Lin, D.; Liang, Z.; Zhao, J.; Yan, K.; Cui, Y. Lithium-coated polymeric matrix as a minimum volume-change and dendrite-free lithium metal anode. *Nature communications* **2016**, *7*, 10992.

(24) Yan, K.; Lu, Z.; Lee, H.-W.; Xiong, F.; Hsu, P.-C.; Li, Y.; Zhao, J.; Chu, S.; Cui, Y. Selective deposition and stable encapsulation of lithium through heterogeneous seeded growth. *Nature Energy* **2016**, *1*, 16010.

(25) Liu, H.; Yue, X.; Xing, X.; Yan, Q.; Huang, J.; Petrova, V.; Zhou, H.; Liu, P. A scalable 3D lithium metal anode. *Energy Storage Materials* **2019**, *16*, 505–511.

(26) Fang, C.; Li, J.; Zhang, M.; Zhang, Y.; Yang, F.; Lee, J. Z.; Lee, M.-H.; Alvarado, J.; Schroeder, M. A.; Yang, Y., et al. Quantifying inactive lithium in lithium metal batteries. *Nature* **2019**, *572*, 511–515.

(27) Wang, X.; Zeng, W.; Hong, L.; Xu, W.; Yang, H.; Wang, F.; Duan, H.; Tang, M.; Jiang, H. Stress-driven lithium dendrite growth mechanism and dendrite mitigation by electroplating on soft substrates. *Nature Energy* **2018**, *3*, 227.

(28) Fang, C.; Wang, X.; Meng, Y. S. Key issues hindering a practical lithium-metal anode. *Trends in Chemistry* **2019**,

(29) Akolkar, R. Mathematical model of the dendritic growth during lithium electrodeposition. *Journal of Power Sources* **2013**, *232*, 23–28.

(30) Monroe, C.; Newman, J. Dendrite growth in lithium/polymer systems a propagation model for liquid electrolytes under galvanostatic conditions. *Journal of the Electrochemical Society* **2003**, *150*, A1377–A1384.

(31) Tartakovsky, D. M.; Xiu, D. Stochastic analysis of transport in tubes with rough walls. *Journal of Computational Physics* **2006**, *217*, 248–259.

(32) Jorne, J.; Lii, Y. J.; Yee, K. E. Suppression of dendrites and roughness during electrodeposition by impinging flow. *Journal of the Electrochemical Society* **1987**, *134*, 1399–1402.

(33) Ehrl, A.; Landesfeind, J.; Wall, W. A.; Gasteiger, H. A. Determination of Transport Parameters in Liquid Binary Lithium Ion Battery Electrolytes I. Diffusion Coefficient. *Journal of The Electrochemical Society* **2017**, *164*, A826–A836.

(34) Zhang, W.; Stone, H. A.; Sherwood, J. Mass transfer at a microelectrode in channel flow. *The Journal of Physical Chemistry* **1996**, *100*, 9462–9464.

(35) Dentry, M. B.; Yeo, L. Y.; Friend, J. R. Frequency effects on the scale and behavior of acoustic streaming. *Physical Review E* **2014**, *89*, 013203.

(36) Länge, K.; Grimm, S.; Rapp, M. Chemical modification of parylene C coatings for SAW biosensors. *Sensors and Actuators B: Chemical* **2007**, *125*, 441–446.

(37) Li, G.; Liu, Z.; Wang, D.; He, X.; Liu, S.; Gao, Y.; AlZahrani, A.; Kim, S. H.; Chen, L.-Q.; Wang, D. Electrokinetic Phenomena Enhanced Lithium-Ion Transport in Leaky Film for Stable Lithium Metal Anodes. *Advanced Energy Materials* **2019**, *9*, 1900704.

(38) Valoen, L. O.; Reimers, J. N. Transport properties of $LiPF_6$-based Li-Ion battery electrolytes. *Journal of the Electrochemical Society* **2005**, *152*, A882.

(39) Diggle, J.; Despic, A.; Bockris, J. The mechanism of the dendritic electrocrystallization of zinc. *Journal of the Electrochemical Society* **1969**, *116*, 1503–1514.

(40) Thielicke, W.; Stamhuis, E. PIVlab—towards user-friendly, affordable and accurate digital particle image velocimetry in MATLAB. *Journal of Open Research Software* **2014**, *2*.

Author contributions

J.F. conceived the idea and supervised the research. A.H. devised and conducted laboratory embodiments to demonstrate its utility and basic principles. H.L. improved the laboratory experiments to obtain better cycling data and directly supervised A.H.'s Li‖Cu cell testing work. O.M. devised, conducted, and wrote the closed-form analysis of the Li^+ ion deposition phenomena. A.H. devised and performed the computational analysis of the SAW-driven flow and Li^+ ion deposition phenomena P.L. supervised H.L. throughout, supervised the advanced battery testing results and interpretation of those results. A.H. wrote the initial and subsequent paper drafts, and produced all experimental data reported within. J.F. heavily revised the paper, and all authors subsequently made final revisions to the paper.

Competing interests

The authors declare no competing interests.